ACS OMEGA

Open Access

http://pubs.acs.org/journal/acsodf

Article

Predicting Iron−Sulfur Cluster Redox Potentials: A Simple Model Derived from Protein Structures

Jiyeon Min, Fidaa Ali, Bernard R. Brooks, Barry D. Bruce, and Muhamed Amin*

Cite This: *ACS Omega* 2025, 10, 15790−15798

Read Online

ACCESS | Metrics & More | Article Recommendations

ABSTRACT: Iron−sulfur (Fe−S) clusters are critical cofactors in metalloproteins, essential for cellular processes such as energy production, DNA repair, enzymatic catalysis, and metabolic regulation. While Fe−S cluster functions are intimately linked to their redox properties, their precise roles in many proteins remain unclear. In this study, we present a regression model based on experimental redox potential (E_m) data, utilizing only two features: the Fe−S cluster's total charge and the Fe atoms' average valence. This model achieves a high correlation with experimental data (R^2 = 0.82) and an average prediction error of 0.12 V. Applying this model across the Protein Data Bank, we predict E_m values for all cataloged Fe−S clusters, uncovering redox potential trends across diverse cluster classes. The computed redox potentials showed strong agreement with experimental values, achieving an overall accuracy of 88%. This streamlined, computationally accessible approach enhances the annotation and mechanistic understanding of Fe−S proteins, offering new insights into the redox variability of electron transport proteins. Our model holds promise for advancing studies of metalloprotein function and facilitating the design of bioinspired redox systems.

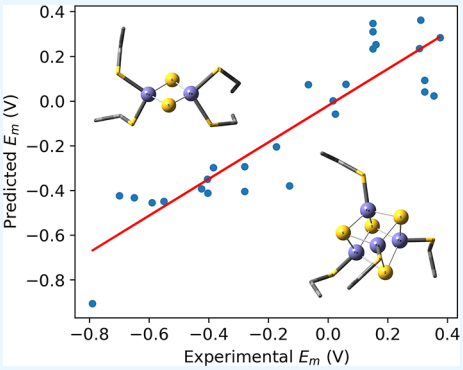

INTRODUCTION

Iron−sulfur (Fe−S) clusters are essential cofactors that maintain structural and catalytic integrity in a wide range of proteins, particularly those involved in fundamental cellular processes.[1−3] As redox-active centers, Fe−S clusters facilitate electron transfer reactions through their capacity to undergo reversible oxidation−reduction transitions. The primary types of these clusters—[1Fe−0S], [2Fe−2S], [4Fe−4S], and [3Fe−4S]—differ in their iron and sulfur atomic configurations, each imparting specific electronic and magnetic properties to the host protein.[4−7] These variations allow Fe−S clusters to modulate their reactivity and interaction specificity, which is critical in enzymes across diverse biological systems. Within cellular contexts, Fe−S clusters are indispensable in key pathways, including oxidative phosphorylation, photosynthetic electron transport, DNA replication, and repair mechanisms.[5,8−13] Their roles extend to enzymes like ferredoxins, aconitase, and ribonucleotide reductase, where the clusters' coordinated iron atoms enable the transfer of electrons critical for metabolic flux and genomic stability. The clusters' unique coordination chemistry also supports their sensitivity to redox fluctuations and oxidative stress, allowing them to act as environmental sensors that can trigger regulatory responses to maintain cellular homeostasis under varying conditions. The lability of Fe−S clusters, especially under oxidative or metal-chelating conditions, underscores their regulatory and signaling roles in dynamic cellular environments. Studying the structural arrangement, electron transfer capabilities, and the biochemical roles of Fe−S clusters deepens our understanding of their multifaceted contributions to cellular function and expands our grasp of the biochemical principles governing protein structure and function in redox biology.[2,14]

The redox properties of the iron centers within Fe−S clusters are primarily responsible for governing their electrochemical characteristics. The redox potential (E_m), a key parameter that reflects the tendency of a molecule to gain or lose electrons, is fundamental to the behavior of iron−sulfur clusters in redox reactions. This potential is intricately determined by the specific number and spatial arrangement of iron and sulfur atoms within each cluster, where configurations such as [2Fe−2S] and [4Fe−4S] provide distinct electronic environments and reactivity profiles.[4,7,15,16] Additionally, the coordination environment of iron atoms—encompassing proximal amino acid residues, solvent molecules, and other ligands—modulates these electrochemical properties by influencing the electron-donating and electron-accepting capabilities of the cluster.[17] The precise arrangement of ligands around the iron centers, including the types and positions of

Received: March 3, 2025
Revised: April 2, 2025
Accepted: April 4, 2025
Published: April 11, 2025

https://doi.org/10.1021/acsomega.5c01976
ACS Omega 2025, 10, 15790−15798

Table 1. Experimental and the Calculated E_m Values of the Different Fe−S Clusters[a]

PDB ID	# Fe	valence	tot. charge	E_m^{exp}[b]	E_m^{calc}	protein name	res.(Å)	organism
1IRO[24]	1	2.950	−2	−0.066[7]	0.073	rubredoxin (oxidized, Fe (III)))	1.1	Clostridium pasteurianum
5NW3[c]	1	2.710	−2	0.016[7]	0.000	rubredoxin	0.59	*Pyrococcus furiosus*
1JM1[25]	2	2.265	−1	0.375[26]	0.284	Rieske FeS protein II (soxf)	1.11	*Sulfolobus acidocaldarius*
1NYK[27]	2	2.475	−1	0.150[28]	0.348	Rieske FeS protein	1.31	*Thermus thermophilus*
1QT9[29]	2	2.935	−3	−0.405[7]	−0.350	ferredoxin	1.3	*Nostoc sp.*
1RFS[30]	2	2.100	−1	0.306[31]	0.234	Rieske FeS protein	1.83	*Spinacia oleracea*
2NUK[32]	2	2.525	−1	0.310[7]	0.363	Rieske FeS protein	1.2	*Rhodobacter sphaeroides*
2PIA[33]	2	3.415	−3	−0.174[33]	−0.205	phthalate dioxygenase reductase	2	*Burkholderia cepacia*
4F1E[34]	2	2.955	−2	0.060[34]	0.074	mitoNEET (D67G)	2.4	*Homo sapiens*
4OO7[35]	2	2.515	−2	0.024[35]	−0.058	Naf-1[2Fe−2S] NEET protein	1.65	*Homo sapiens*
4OOA[35]	2	3.120	−3	−0.280[35]	−0.294	Naf1(MINER1): H114C	1.58	*Homo sapiens*
8HN2[36]	2	2.350	−1	0.150[36]	0.310	Rieske FeS protein	2.3	*Chlorobaculum tepidum*
1FXD[37]	3	2.840	−3	−0.130[7]	−0.379	ferredoxin II	1.7	*Desulfovibrio gigas*
5FD1[d38]	3	2.793	−3	−0.425[7]	−0.393	ferredoxin	1.9	*Azotobacter vinelandii*
5FD1[d38]	4	2.662	−3	−0.650[7]	−0.432	ferredoxin	1.9	*Azotobacter vinelandii*
1CKU[39]	4	2.788	−2	0.355[7]	0.024	high potential iron protein	1.2	*Allochromatium vinosum*
1FXR[40]	4	3.105	−3	−0.385[7]	−0.298	ferredoxin I	2.3	*Desulfovibrio africanus*
1G5P[41]	4	2.478	−4	−0.790[42]	−0.906	nitrogenase Iron Protein	2.2	*Azobacter vinelandii*
1IQZ[43]	4	2.752	−3	−0.280[7]	−0.405	ferredoxin	0.92	*Bacillus thermoproteolyticus*
1JB0[d44]	4	2.610	−3	−0.550[12]	−0.448	ferredoxin	2.5	*Synechococcus elongatus*
1JB0[d44]	4	2.588	−3	−0.590[12]	−0.455	ferredoxin	2.5	*Synechococcus elongatus*
1JB0[d44]	4	2.690	−3	−0.700[12]	−0.424	Fferredoxin	2.5	*Synechococcus elongatus*
1VJW[45]	4	2.732	−3	−0.404[46]	−0.411	oxidoreductase	1.75	*Thermotoga maritima*
2HIP[47]	4	3.482	−2	0.150[7]	0.234	high potential FeS protein	2.5	*Halorhodospira halophila*
3A39[48]	4	2.845	−2	0.323[48]	0.041	high potential FeS protein	0.72	*Thermochromatium tepidum*
4RR2[49]	4	3.545	−2	0.160[50]	0.253	human primase	2.65	*Homo sapiens*
7VOS[51]	4	3.015	−2	0.323[51]	0.093	high potential FeS protein	1.2	*Thermochromatium tepidum*

[a]The valences are calculated based on the coordinates in the PDB files. The total charges include the Fe, the bridging S, and the Cystine S. [b]All redox potential values are reported relative to the standard hydrogen electrode (SHE), as specified in the cited references. [c]The reference for this structure is currently in press, but the structural data is available in the PDB. [d]Entries sharing the same PDB ID represent the same protein structure, with each E_m value corresponding to a different Fe−S cluster.

coordinating amino acids, can substantially affect the clusters' redox activity by stabilizing certain oxidation states over others. Furthermore, external factors such as the overall spin state of the cluster, ambient pH, temperature, and the presence of other molecules or cofactors in the cellular milieu can significantly alter the redox potential and electron transfer kinetics. Variations in these conditions can dynamically impact the clusters' function, affecting critical cellular processes like respiration and DNA repair. Despite the recognized influence of each factor, the relative contributions of these elements to the overall redox chemistry of Fe−S clusters remain to be fully quantified. It is unclear whether certain variables consistently dominate in determining the electrochemical profile of Fe−S clusters, highlighting a need for further studies to dissect their individual and combined roles in modulating cluster reactivity and stability.

Numerous studies have utilized quantum mechanical (QM) methods, particularly those based on Density Functional Theory (DFT), to estimate the E_m of Fe−S clusters.[7,15,16,18−21] These QM methods offer in-depth insights into the electronic and structural factors affecting redox behavior and can capture subtle interactions such as spin coupling, charge delocalization, and solvent effects. However, these approaches face significant challenges when applied to Fe−S clusters, which are highly sensitive to protein electrostatics, solvation effects, and complex electronic structures involving charge delocalization and mixed valence states. While these calculations often correlate with experimental redox potentials, they frequently exhibit substantial absolute errors, sometimes exceeding 0.17 V.[7] Moreover, attempts to estimate redox potentials using DFT calculations in vacuum, followed by corrections via Poisson−Boltzmann solvation models, have reported errors ranging from 0.1 to 0.3 V compared to experimental values.[22] Additionally, these quantum mechanical approaches are computationally demanding, requiring significant processing power and resources. In contrast, our data-driven model directly learns from experimentally measured redox data, reducing reliance on parameters such as functionals, basis sets, and other variables that can introduce systematic offsets in DFT. A key insight of our approach is that many structures deposited in the Protein Data Bank (PDB) may be photoreduced during X-ray data collection, effectively representing reduced states. This issue was highlighted by Kapuścińska et al.,[23] who applied a machine learning model to over 30,000 metalloproteins in the PDB and found that metals are predominantly in reduced states, likely due to photoreduction during radiation exposure. This suggests that even when the biological system originally contained oxidized clusters, the structures archived in the PDB often reflect their reduced forms instead.

In this study, we aimed to develop a simpler and computationally efficient predictive model for Fe−S cluster redox potentials. Using a multiple linear regression approach, our model relies on only two primary features: the net charge

https://doi.org/10.1021/acsomega.5c01976
ACS Omega 2025, 10, 15790−15798

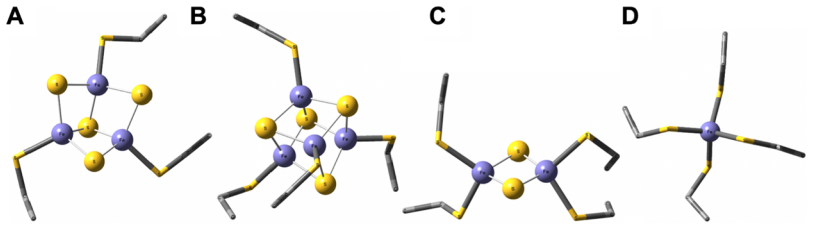

Figure 1. Structure of different Fe−S centers. (A) 3Fe−4S cluster of the 5FD1 PDB structure, (B) 4Fe−4S cluster of the 2HIP PDB, (C) 2Fe−2S structure of the 2PIA PDB, and (D) 1F−0S cluster of the 1IRO PDB.

of the cluster and the average valence of the Fe atoms. The valence provides information on the Fe-ligand bond length and the ligand's atom type, reflecting variations observed in some proteins where a His ligand replaces a Cys ligand. The model was trained and validated against a data set of experimentally determined redox potentials from a variety of Fe−S clusters in protein environments. By analyzing the regression coefficients, we assessed the relative importance of each feature, offering insights into how these factors contribute to the redox chemistry of Fe−S clusters. Following validation, we applied our model to predict the redox potentials of all Fe−S clusters cataloged in the PDB, encompassing clusters with 1 to 4 Fe atoms. This approach, tested on 27 distinct Fe−S clusters from the PDB, demonstrates the potential of a streamlined, data-driven model for effectively estimating redox potentials and guiding further experimental and theoretical investigations.

METHODS

Data Preparation. In this study, 27 unique Fe−S containing proteins were selected from the PDB, representing a diverse array of Fe−S cluster configurations and host organisms. The choice of this reference set was deliberately designed to include diverse organism types and a range of resolutions, which enhances the generalizability of our model across different biological systems. The data set includes proteins with distinct Fe configurations: two examples with 1 Fe, ten examples with 2 Fe, two examples with 3 Fe, and 13 examples with 4 Fe atoms in their clusters. Each structure was determined using X-ray diffraction (XRD) with resolutions ranging from 0.59 to 2.65 Å. To ensure data quality, we excluded structures with resolutions worse than 2.7 Å, which are too low for reliable analysis. While we cautiously included data in the 2.5−2.7 Å range, we aimed not to miss valuable redox potential data. For example, structure 4RR2 with the lowest resolution in our data set (2.65 Å) was specifically included due to its distinct functional role in human primase, which is involved in DNA replication rather than typical electron transport. These proteins span a broad phylogenetic spectrum, encompassing 22 prokaryotic and 5 eukaryotic sources, as outlined in Table 1, forming a robust training set. Figure 1 illustrates examples of Fe−S clusters in the data set: (a) a 3Fe−4S cluster from PDB structure 5FD1, (b) a 4Fe−4S cluster from PDB 2HIP, (c) a 2Fe−2S cluster from PDB 2PIA, and (d) an Fe-Cys cluster from PDB 1IRO.

Features Selection. The limited data set necessitated careful feature selection to avoid model overfitting. Fe−S clusters exhibit numerous structural and chemical properties that can serve as features, including Fe atom count, reduced Fe quantity, sulfur ligand count, Fe−S and Fe−Fe bond distances, total spin state, and the local protein environment. Most of these features are strongly correlated. For example, the total spin correlates with the total charge of the cluster which in turn correlates with cluster geometry.

To ensure computational simplicity and broad applicability, three primary features were selected, avoiding those derived from quantum computational methods such as DFT. While DFT-based features have shown promising correlations with experimental electrochemical data, they often involve significant computational costs and can yield substantial absolute errors in redox potential predictions. For example, DFT-based QM/MM approaches have reported mean absolute deviations of approximately 0.17 V, even after applying a systematic error correction of −0.55 V.[7] Additionally, challenges in disentangling the contributions of cluster geometry, spin states, charge distribution, and the protein environment complicate DFT-based predictions. To address these limitations, features were directly derived from atomic coordinates, avoiding the computational complexity of DFT while enabling broader applicability to larger data sets and diverse systems.

Three key features were extracted from 27 PDB entries:

1. Average Fe−S bond lengths: The mean of all Fe-ligand distances in the cluster.[23]
2. Total charge in the reduced state: Reflecting the overall electronic distribution of the cluster in its reduced form.
3. Average valence: Quantifying the oxidation state of Fe atoms based on Fe-ligand distances and ligand types.

Structures deposited in the PDB may undergo photoreduction during X-ray data collection, thereby predominantly representing reduced redox states. The assumption that all PDB structures correspond to reduced states serves as a computational simplification that offers a consistent reference framework. Under this assumption, definitive charges can be assigned to iron atoms within the clusters, which is essential for accurate calculation of the total cluster charge. Since we cannot definitively determine whether crystal structures represent oxidized states, reduced states, or mixtures, adopting the reduced state assumption allows for uniform comparison across diverse structures.

The average valence of an Fe−S cluster provides insight into its overall redox characteristics. The valence of each Fe center is calculated using the bond valence model:

$$v = \sum_i e^{(R_0 - R_i)/B} \tag{1}$$

where R_0 and B are empirical parameters derived from the International Union of Crystallography (IUCr) data set, as determined by David Brown. R_0 represents the ideal bond distance for a specific ligand and oxidation state, while R_i represents the observed bond distance between the metal center and ligand i.[52,53]

The oxidation state of each Fe atom is assigned by rounding the computed valence to the nearest integer after calculating

https://doi.org/10.1021/acsomega.5c01976
ACS Omega 2025, 10, 15790−15798

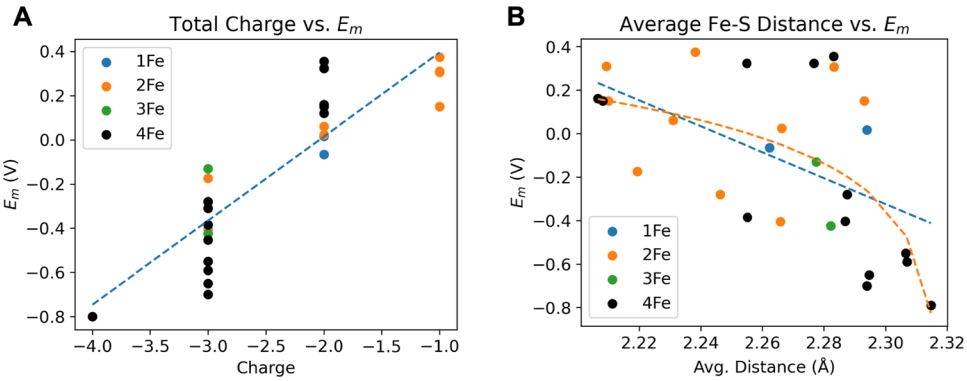

Figure 2. Correlation of E_m with charge and average Fe−S distance. Each data point represents an iron−sulfur cluster, with colors indicating the number of Fe atoms (1Fe, 2Fe, 3Fe, or 4Fe), as shown in the legend. (A) Correlation between E_m (V) and the total charges of the cluster in the reduced state. The data were fitted using linear regression, resulting in a linear fit (R^2 = 0.74, blue line) with best-fit coefficients a_0= 0.77 and a_1= 0.38. (B) Correlation between E_m (V) and the average Fe−S bond distance (Å). The data were fitted using linear regression, yielding a linear fit (R^2 = 0.30, blue line) with best-fit coefficients a_0= 13.40 and a_1= −5.97. Additionally, a logarithmic fit (R^2 = 0.39, orange line) was obtained using eq 2, with coefficients a_0 = 0.27, a_1 = 37.21, and a_2 = 16.05.

the valence for both its higher and lower oxidation states using the appropriate R_0 values. This process is repeated for all Fe atoms within the cluster, and the average valence is calculated to provide an overall measure of the cluster's redox characteristics.

By deriving features directly from atomic coordinates, this method ensures computational efficiency and scalability while maintaining accuracy across diverse Fe−S cluster types. This approach represents a practical alternative to computationally intensive DFT-based methods, making it well-suited for large-scale studies of redox systems.

Machine Learning Models. The modeling process for predicting E_m is conducted in stages, progressively refining the framework through systematic feature selection and performance evaluation. Initially, a baseline linear regression model is considered, using total charge (x) and as the sole predictor (Figure 2A). Recognizing the limited predictive power of total charge alone, the feasibility of using the average Fe−S bond distance as a complementary feature is tested (Figure 2B).

A nonlinear dependence is observed for the average Fe−S bond distance (Figure 2B). Thus, a logarithmic model is also introduced to include the nonlinear effect of the bond length (eq 2).

$$E_m = a_0 + a_1 x_1 + a_2 \log(a_3 - a_4 \cdot x_2) \quad (2)$$

A comparative evaluation of the coefficient of determination (R^2) values between the linear and nonlinear models reveals negligible differences, indicating that a linear formulation adequately captures the relationship between the features and E_m. Furthermore, replacing the average distances by the average valence yields a better agreement with the experiment.

The scikit-learn Python library is used for efficient training and evaluation. Model performance is assessed using R^2 and mean absolute error (MAE), which provide a comprehensive understanding of both the model's explanatory power and predictive accuracy.

To rigorously evaluate the model's reliability, Monte Carlo cross-validation was conducted with 1000 iterations. In each iteration, the data set was randomly split, with 70% (19 structures) used for training and 30% (8 structures) for testing. This cross-validation approach serves two key purposes: (1) to ensure the model's performance is not dependent on specific data points, and (2) to verify that lower-resolution structures do not negatively influence the results.

Application of the Model to Protein Structures in PDB. The developed model is applied to predict E_m values of Fe−S clusters across all protein structures in the PDB, enabling a comprehensive, large-scale analysis of redox properties. Python scripts are implemented to automate data extraction and calculations using the Biopython library, allowing efficient parsing of PDB files, determination of average valences, and calculation of total charges for each cluster.

To define cluster charges, sulfur atoms were assigned specific values. Cysteine-linked sulfurs were set at −1, while bridging sulfurs, which connect iron atoms, were assigned a charge of −2. Given the redox activity of Fe−S clusters, each iron atom can shift between oxidation states, allowing clusters to cycle between reduced and oxidized forms during protein function. However, in this study, only the reduced iron state was considered.

Each Fe−S cluster type corresponds to specific protein classes. The [1Fe−0S] cluster is exclusively found in Rubredoxin, where iron alternates between +2 (reduced) and +3 (oxidized) states. The [2Fe−2S] cluster appears in two classes: Ferredoxin, coordinated by four cysteine-derived sulfurs, and Rieske, coordinated by two cysteine sulfurs and two histidine ligands. The [3Fe−4S] cluster is found solely in Ferredoxin. The [4Fe−4S] cluster appears in two classes: Ferredoxin, where all four sulfur atoms are provided by cysteine residues, and High-Potential Iron−Sulfur Protein (HiPIP), where three cysteine residues and one additional ligand coordinate the cluster.

The data set used in this analysis comprises 9821 Fe−S clusters from over 3800 PDB structures, representing a comprehensive range of protein environments. Among them, 232 [1Fe−0S] Rubredoxin clusters were identified from 142 structures, 1625 [2Fe−2S] Ferredoxin clusters from 723 structures, and 902 [2Fe−2S] Rieske clusters from 407 structures. The data set also included 680 [3Fe−4S] Ferredoxin clusters from 333 structures, 5055 [4Fe−4S] Ferredoxin clusters from 1476 structures, and 1327 [4Fe−4S] HiPIP clusters from 799 structures.

The predicted E_m values are analyzed to identify patterns and trends across the data set. Distributions of redox potentials for each cluster type are examined to reveal their variability and

https://doi.org/10.1021/acsomega.5c01976
ACS Omega 2025, 10, 15790−15798

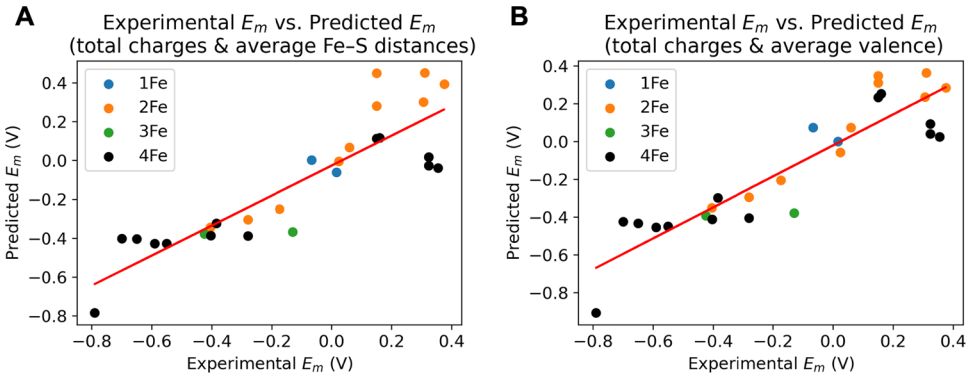

Figure 3. Comparison between calculated and experimental E_m. (A) Data were fitted using the total charge and average Fe−S bond distance as predictors. The best-fit coefficients are a_0 = 5.27, a_1 = 0.34, and a_2=-2.03, resulting in R^2 = 0.77. (B) Data were fitted with total charge and average valence as predictors. The best-fit coefficients are a_0 = 0.02, a_1 = 0.42, and a_2 = 0.30, yielding R^2 = 0.82.

explore how structural and chemical diversity influence redox properties. This approach allows for a global assessment of Fe−S clusters, uncovering the range and characteristics of their electrochemical behavior in various protein contexts.

RESULTS AND DISCUSSION

In this study we present a simple linear regression model that predicts the redox potential of Fe−S based on experimental measurements. We outline the stepwise refinement of predictive models for Fe−S cluster redox potential (E_m) starting with total charge as a baseline feature. The model was progressively refined by incorporating additional features such as average Fe−S bond lengths and average valence, ultimately resulting in a robust and accurate final model.

The analysis began with total charge as the sole predictor, revealing a moderate linear relationship with E_m (R^2 = 0.74), as shown in Figure 2A. Lower total charge values correspond to lower E_m, a trend consistently observed across Fe−S cluster types. Notably, [4Fe−4S] clusters demonstrate a broader capacity for redox tuning, which is expected due to their greater number of Fe centers, allowing for more extensive electrochemical adjustments within protein environments. Most experimental data points fall within clusters with total charges of −3 and −2, highlighting these as common configurations in biological systems.[54]

Despite the moderate linear relationship between total charge and E_m, substantial variability in E_m values exist within individual charge states. For example, clusters with a total charge of −3 have an average E_m of −0.41 V, but the standard deviation is ±0.18 V, indicating significant spread. Similarly, clusters with a charge of −2 average 0.15 V with a standard deviation of ±0.15 V. This variability suggests that total charge alone is insufficient to fully explain the differences in E_m across Fe−S clusters, highlighting the need for additional features to capture structural and electronic diversity.

To address this, average Fe−S bond lengths were introduced as an additional feature to provide insight into the electronic structure of the cluster, as shorter bonds generally indicate more oxidized states. Using the average value of bond lengths, rather than individual bond lengths, simplifies the model and enhances computational efficiency. Since Fe−S clusters vary in the number of Fe atoms and ligands, incorporating all individual bond lengths as features could introduce inconsistencies and increase the risk of overfitting. Averaging bond lengths reduces structural complexity while retaining essential information about the cluster's electronic environment.

Figure 2B shows that longer average Fe−S bond lengths correspond to lower E_m values, but the correlation was weak (R^2 = 0.30). To explore whether nonlinear dependencies between bond lengths and E_m could improve the model, a logarithmic adjustment (eq 2) was applied, accounting for the diminishing influence of bond length changes on E_m. This adjustment resulted in a modest improvement in performance (R^2 = 0.39) but demonstrated that bond lengths alone remain insufficient for reliable predictions.

These findings emphasize that neither total charge nor the average bond length alone can fully capture the complexity of redox potential predictions. Together, they suggest the importance of integrating multiple features to account for both the electronic and structural variability of Fe−S clusters.

To address the limitations of single-feature models, a composite linear model combining total charge and average bond length was developed. These models achieved R^2 values of 0.79 and 0.77 (Figure 3A), respectively, demonstrating that integrating structural and electronic features significantly improves predictive accuracy. After testing both options and observing their R^2 values to be nearly equivalent, the linear composite model was selected due to its simplicity and nearly identical performance to the nonlinear alternative, making it an optimal choice for further development.

Despite the composite model's moderate performance, Fe−S bond lengths have inherent limitations as a feature. They do not account for variations in ligand types, such as nitrogen ligands replacing sulfur, which can significantly influence redox potential. To address this, average valence (eq 1) was introduced as a new feature. Average valence incorporates both Fe-ligand distances and ligand types into a single descriptor, providing a comprehensive representation of the chemical environment and oxidation state of Fe atoms. By including empirical adjustments (e.g., R_0) to account for ligand type differences, the bond valence model allows average valence to capture structural and electronic variations more effectively. This makes average valence a more comprehensive and descriptive feature than bond lengths alone.

The final linear regression model, combining total charge and average valence as predictors, demonstrates exceptional performance. Trained on data from all 27 PDB entries (Table 1), this model achieved the highest predictive accuracy, with a R^2 of 0.82 and a MAE of 0.12 V:

https://doi.org/10.1021/acsomega.5c01976
ACS Omega 2025, 10, 15790−15798

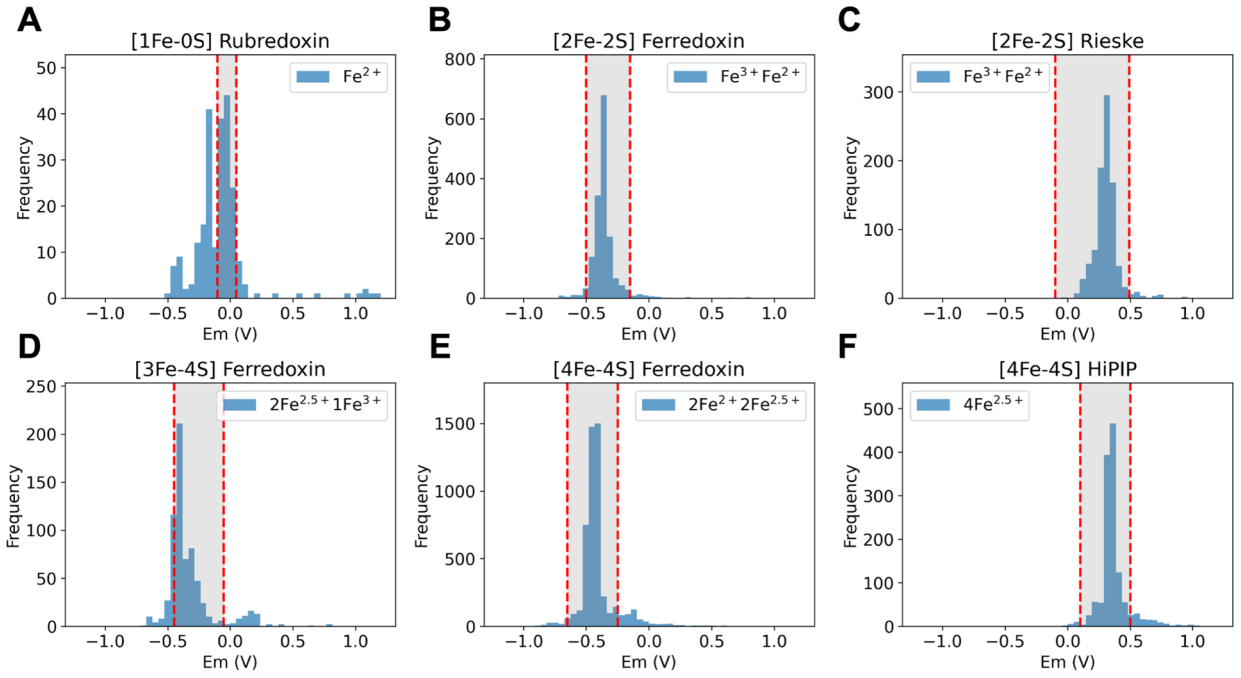

Figure 4. Application of the model to Fe−S cluster-containing proteins. Computed redox potential (E_m) histograms are shown, with shaded regions indicating experimentally determined values for (A) [1Fe−0S], (B) [2Fe−2S] ferredoxin, (C) [2Fe−2S] Rieske, (D) [3Fe−4S], (E) [4Fe−4S] ferredoxin, and (F) [4Fe−4S] HiPIP clusters. The model demonstrates high accuracy (>85%) for [2Fe−2S] Ferredoxin, [2Fe−2S] Rieske, [4Fe−4S] Ferredoxin, and [4Fe−4S] HiPIP, while lower accuracy is observed for [1Fe−0S] Rubredoxin (46%) and [3Fe−4S] Ferredoxin (78%).

$$E_m = 0.02 + 0.42\cdot(\text{total charge}) + 0.30\cdot(\text{average valence}) \quad (3)$$

The model's predicted E_m values show a strong correlation with experimental measurements, as illustrated in Figure 3B. A key factor in the model's success is the inclusion of average valence, which captures both structural and electronic characteristics of Fe−S clusters. By integrating total charge and average valence, the model accurately predicts E_m values across a diverse range of Fe−S cluster types, demonstrating its applicability to a variety of biochemical systems.

Model Evaluations. The final model demonstrates robust predictive performance, achieving an average R^2 value of 0.73 ± 0.14 and a MAE of 0.14 ± 0.03 V through rigorous cross-validation testing, outperforming existing methods in predictive accuracy. The consistent performance across cross-validation iterations (1000 random 70/30 splits) indicates minimal impact from resolution constraints. Particularly noteworthy is the small standard deviation in MAE (only 0.03 V), which demonstrates that our model maintains reliable performance regardless of which specific structures are included in each iteration.

If low-resolution structures were significantly problematic for our analysis, we would observe much higher variance in our error metrics as different subsets of the data were used for training and testing. This robustness suggests that our approach effectively captures the essential determinants of redox potential across diverse Fe−S cluster systems, regardless of minor variations in structural resolution.

To further evaluate the contribution of each feature, scaled regression coefficients were analyzed. Scaling was performed to ensure comparability, as total charge and average valence operate on different numerical ranges. After scaling, total charge exhibited a coefficient of 0.34, underscoring its dominant role in determining E_m. In contrast, average valence, with a smaller coefficient of 0.10, provided additional precision by capturing ligand-specific effects and structural variability.

Together, these features enable accurate and interpretable predictions of Fe−S cluster redox potentials, balancing simplicity and predictive power while offering insights into the structural and electronic factors influencing redox behavior.

The resolution of different structures varies, leading to potential differences in error when calculating redox potential. Although the resulting error is small and not critical for the conclusions of our study, it can be estimated if necessary. Specifically, the error in average bond length measurements can be approximated as 10% of the resolution.[55,56] Using a Taylor series approximation, this error can be propagated to the calculated E_m values according to the following equation: $\Delta E_m(x) = E_m'(x)\Delta x$, where x is the average bond length, Δx is the error in the measured bond length (0.1 of the resolution) and E_m' is the derivatives of the E_m with respect to the average bond length.

Model-Based Redox Potentials of Fe−S Clusters: Global Trends and Validation. Following model evaluation, the optimized version was applied to predict E_m values of Fe−S clusters across all protein structures in the PDB. E_m values were computed using eq 3, with the analysis focusing on the four most prevalent Fe−S cluster types: [1Fe−0S], [2Fe−2S], [3Fe−4S], and [4Fe−4S].

The computed E_m distributions were visualized as histograms (Figure 4), illustrating the spread of E_m values for each Fe−S cluster class. These distributions exhibit an approximately normal shape, suggesting that redox potentials are relatively well-defined within each cluster type.

Table 2 summarizes the mean E_m values and standard deviations for each Fe−S cluster type, providing a clearer understanding of redox trends. Ferredoxin-type clusters exhibit consistently negative redox potentials, with values of −0.35 V for [2Fe−2S] Ferredoxin, −0.33 V for [3Fe−4S] Ferredoxin,

https://doi.org/10.1021/acsomega.5c01976
ACS Omega 2025, 10, 15790−15798

Table 2. Mean E_m Values and Standard Deviation Values for Each Fe−S Cluster Classes

cluster	class	redox state	mean E_m (mV)	st. dev.
1Fe−0S	rubredoxin	$Fe^{2+/3+}$	−0.06	0.31
2Fe−2S	ferredoxin	$[2Fe-2S]^{1+/2+}$	−0.35	0.12
	rieske	$[2Fe-2S]^{1+/2+}$	0.31	0.14
3Fe−4S	ferredoxin	$[3Fe-4S]^{0/1+}$	−0.33	0.22
4Fe−4S	ferredoxin	$[4Fe-4S]^{1+/2+}$	−0.40	0.27
	HiPIP	$[4Fe-4S]^{2+/3+}$	0.37	0.13

and −0.40 V for [4Fe−4S] Ferredoxin, reinforcing their role as electron donors in biological reduction reactions. In contrast, Rieske [2Fe−2S] and HiPIP [4Fe−4S] clusters display positive redox potentials of 0.31 and 0.37 V, respectively, consistent with their function as high-potential electron carriers. The [1Fe−0S] Rubredoxin cluster, with a mean E_m of −0.06 V, exhibits a near-neutral redox potential, suggesting a more balanced redox behavior compared to other Fe−S clusters. Across all clusters, standard deviations range from 0.12 to 0.31 V, indicating that while some variability exists, redox potentials remain within a predictable range for each class.

To assess the alignment between computed E_m values and experimentally determined redox potentials,[54,57−60] their distributions were compared. As shown in Figure 4, the histogram illustrates the computed redox potential distributions for different Fe−S clusters, with experimentally determined values highlighted in the shaded area. The degree of agreement was quantified as the percentage of computed values falling within the experimental range, calculated using the formula (number of computed values within the experimental range/total number of data points) × 100.

The computational results show an 87.78% agreement with experimental values, matching in 8621 out of 9821 cases. Strong agreement was observed for most Fe−S cluster types: [2Fe−2S] Ferredoxin (93.66%, 1522/1625), [2Fe−2S] Rieske (96.67%, 872/902), [4Fe−4S] Ferredoxin (87.06%, 4401/5055), and [4Fe−4S] HiPIP (89.75%, 1191/1327), with over 85% of computed values within the experimentally determined range. This high level of agreement suggests that the model effectively captures key electronic and structural features influencing redox potential, particularly for Fe−S clusters with well-defined oxidation states and stable coordination environments.

For [1Fe−0S] Rubredoxin (46.12%, 107/232) and [3Fe−4S] Ferredoxin (77.65%, 528/680), the computed values showed a broader distribution relative to experimental measurements, leading to a lower percentage of agreement. This difference may be attributed to greater structural variability or additional electronic factors influencing redox potential that are not explicitly accounted for in the current computational framework. However, rather than indicating a fundamental inaccuracy in the model, these results suggest that additional refinement of the model's parametrization could enhance agreement for these specific cluster types.

Overall, the computed redox potentials exhibit a strong correlation with experimental values for most Fe−S clusters, particularly those with well-characterized electronic properties. Further refinement of the computational framework, incorporating a more detailed representation of local structural variations and environmental effects, may improve agreement for Fe−S clusters exhibiting a broader range of redox potentials.

CONCLUSIONS

Predicting the midpoint potential (E_m) of Fe−S clusters is essential for understanding the mechanics of electron transport across diverse biological systems. Fe−S clusters, integral to many electron transport proteins from mitochondrial respiratory complexes to photosynthetic reaction centers, function as redox-active sites, transferring electrons with precision and efficiency. The model developed in this study presents a streamlined yet accurate approach to predicting E_m values, bridging a gap left by more complex computational methods. By utilizing readily obtainable structural and electronic features, total charge and average valence, this method achieves high predictive accuracy without the heavy computational cost typically associated with quantum mechanical approaches such as DFT. This simplicity and accessibility make it feasible to apply the model on a large scale, such as across all Fe−S clusters in the PDB, thereby greatly enhancing our ability to annotate the redox behavior of proteins with currently unknown E_m values.

This study's accessible and efficient model enriches the field of structural bioinformatics by linking fundamental structural parameters with redox function, providing a tool that is as straightforward as it is effective. As protein structure databases expand, this model offers researchers the opportunity to predict electron transfer characteristics across newly resolved protein structures, fostering discoveries in redox biology. The simplicity of this approach also supports studies on redox-sensitive signaling and cellular response mechanisms, where Fe−S cluster E_m values may serve as regulatory switches under oxidative or reductive stress conditions. By integrating simplicity with scientific rigor, this work positions itself as an essential tool for exploring cellular responses to environmental changes, with implications ranging from microbial redox physiology to human health. Despite the strong overall agreement (87.78%) with experimental E_m values, the model exhibits lower accuracy for certain clusters, particularly [1Fe−0S] Rubredoxin and [3Fe−4S] Ferredoxin, highlighting the influence of structural or electronic factors not fully captured by this simplified approach. These cases highlight the importance of refining the model or complementing it with more detailed quantum mechanical methods when addressing complex Fe−S clusters.

In summary, this study's predictive model of Fe−S cluster E_m's offers a computationally accessible and simplified yet powerful method that advances our understanding of redox variability across electron transport systems. Its capacity for large-scale application, combined with its straightforward methodology, opens new doors in the fields of functional annotation, mechanistic exploration, and bioengineering. This approach enhances the field of biological electron transport, offering unprecedented insights into the functional diversity of Fe−S clusters across life's broad spectrum.

AUTHOR INFORMATION

Corresponding Author

Muhamed Amin − *Laboratory of Computational Biology, National Heart, Lung, and Blood Institute, National Institutes of Health, Bethesda, Maryland 20892, United States; Department of Sciences, University College Groningen, University of Groningen, 9718 BG, Groningen, The*

https://doi.org/10.1021/acsomega.5c01976
ACS Omega 2025, 10, 15790−15798

Netherlands; orcid.org/0000-0002-3146-150X; Email: Muhamed.amin@nih.gov

Authors

Jiyeon Min − *Laboratory of Computational Biology, National Heart, Lung, and Blood Institute, National Institutes of Health, Bethesda, Maryland 20892, United States; Biophysics Program, Institute for Physical Science and Technology, University of Maryland, College Park, Maryland 20742, United States;* orcid.org/0009-0006-8086-095X

Fidaa Ali − *Bredesen Center for Interdisciplinary Research and Graduate Education, Genome Science and Technology Program, University of Tennessee, Knoxville, Tennessee 37996, United States;* orcid.org/0000-0002-2646-073X

Bernard R. Brooks − *Laboratory of Computational Biology, National Heart, Lung, and Blood Institute, National Institutes of Health, Bethesda, Maryland 20892, United States;* orcid.org/0000-0002-3586-2730

Barry D. Bruce − *Bredesen Center for Interdisciplinary Research and Graduate Education, Genome Science and Technology Program and Department of Biochemistry & Cellular and Molecular Biology, University of Tennessee, Knoxville, Tennessee 37996, United States;* orcid.org/0000-0002-4045-9815

Complete contact information is available at: https://pubs.acs.org/10.1021/acsomega.5c01976

Notes

The authors declare no competing financial interest.

■ ACKNOWLEDGMENTS

This work was supported by the National Heart, Lung and Blood Institute (NHLBI) at the National Institute of Health for J.M., B.R.B. and M.A. In addition, it was partially supported by the Graduate Advancement, Training, and Education (GATE) award from the University of Tennessee-Oak Ridge Innovation Institute (UT-ORII) to F.A. and B.D.B.

■ REFERENCES

(1) Holm, R. H.; Lo, W. Structural Conversions of Synthetic and Protein-Bound Iron-Sulfur Clusters. *Chem. Rev.* **2016**, *116* (22), 13685−13713.

(2) Fontecave, M.; Py, B.; Ollagnier de Choudens, S.; Barras, F. From Iron and Cysteine to Iron-Sulfur Clusters: the Biogenesis Protein Machineries. *EcoSal Plus* **2008**, *3* (1), 14.

(3) Barthelme, D.; Scheele, U.; Dinkelaker, S.; Janoschka, A.; Macmillan, F.; Albers, S. V.; Driessen, A. J.; Stagni, M. S.; Bill, E.; Meyer-Klaucke, W.; et al. Structural organization of essential iron-sulfur clusters in the evolutionarily highly conserved ATP-binding cassette protein ABCE1. *J. Biol. Chem.* **2007**, *282* (19), 14598−14607.

(4) Banci, L.; Bertini, I.; Ciurli, S.; Ferretti, S.; Luchinat, C.; Piccioli, M. The electronic structure of [Fe4S4]3+ clusters in proteins. An investigation of the oxidized high-potential iron-sulfur protein II from Ectothiorhodospira vacuolata. *Biochemistry* **1993**, *32* (36), 9387−9397.

(5) Nasta, V.; Suraci, D.; Gourdoupis, S.; Ciofi-Baffoni, S.; Banci, L. A pathway for assembling [4Fe-4S](2+) clusters in mitochondrial iron-sulfur protein biogenesis. *FEBS J.* **2020**, *287* (11), 2312−2327.

(6) Netz, D. J.; Genau, H. M.; Weiler, B. D.; Bill, E.; Pierik, A. J.; Lill, R. The conserved protein Dre2 uses essential [2Fe-2S] and [4Fe-4S] clusters for its function in cytosolic iron-sulfur protein assembly. *Biochem. J.* **2016**, *473* (14), 2073−2085.

(7) Jafari, S.; Tavares Santos, Y. A.; Bergmann, J.; Irani, M.; Ryde, U. Benchmark Study of Redox Potential Calculations for Iron-Sulfur Clusters in Proteins. *Inorg. Chem.* **2022**, *61* (16), 5991−6007.

(8) Mannan, R. M.; He, W. Z.; Metzger, S. U.; Whitmarsh, J.; Malkin, R.; Pakrasi, H. B. Active photosynthesis in cyanobacterial mutants with directed modifications in the ligands for two iron-sulfur clusters on the PsaC protein of photosystem I. *EMBO J.* **1996**, *15* (8), 1826−1833.

(9) Noodleman, L.; Lovell, T.; Liu, T.; Himo, F.; Torres, R. A. Insights into properties and energetics of iron-sulfur proteins from simple clusters to nitrogenase. *Curr. Opin Chem. Biol.* **2002**, *6* (2), 259−273.

(10) Petronek, M. S.; Spitz, D. R.; Allen, B. G. Iron-Sulfur Cluster Biogenesis as a Critical Target in Cancer. *Antioxidants* **2021**, *10* (9), 1458.

(11) Teo, R. D.; Migliore, A.; Beratan, D. N. Mutation effects on charge transport through the p58c iron-sulfur protein. *Chem. Sci.* **2020**, *11* (27), 7076−7085.

(12) Vassiliev, I. R.; Antonkine, M. L.; Golbeck, J. H. Iron-sulfur clusters in type I reaction centers. *Biochim. Biophys. Acta* **2001**, *1507* (1−3), 139−160.

(13) Weiner, B. E.; Huang, H.; Dattilo, B. M.; Nilges, M. J.; Fanning, E.; Chazin, W. J. An iron-sulfur cluster in the C-terminal domain of the p58 subunit of human DNA primase. *J. Biol. Chem.* **2007**, *282* (46), 33444−33451.

(14) Liu, L.; Huang, M. Essential role of the iron-sulfur cluster binding domain of the primase regulatory subunit Pri2 in DNA replication initiation. *Protein Cell* **2015**, *6* (3), 194−210.

(15) Ali, F.; Shafaa, M. W.; Amin, M. Computational Approach for Probing Redox Potential for Iron-Sulfur Clusters in Photosystem I. *Biology* **2022**, *11* (3), 362.

(16) Blachly, P. G.; Sandala, G. M.; Giammona, D. A.; Bashford, D.; McCammon, J. A.; Noodleman, L. Broken-Symmetry DFT Computations for the Reaction Pathway of IspH, an Iron-Sulfur Enzyme in Pathogenic Bacteria. *Inorg. Chem.* **2015**, *54* (13), 6439−6461.

(17) Kassner, R. J.; Yang, W. A theoretical model for the effects of solvent and protein dielectric on the redox potentials of iron-sulfur clusters. *J. Am. Chem. Soc.* **1977**, *99* (13), 4351−4355.

(18) Canty, A. J.; Ariafard, A.; Puddephatt, R. J. DFT studies of two-electron oxidation, photochemistry, and radical transfer between metal centres in the formation of platinum(IV) and palladium(IV) selenolates from diphenyldiselenide and metal(II) reactants. *Dalton Trans* **2020**, *49* (39), 13566−13572.

(19) de la Lande, A.; Alvarez-Ibarra, A.; Hasnaoui, K.; Cailliez, F.; Wu, X.; Mineva, T.; Cuny, J.; Calaminici, P.; Lopez-Sosa, L.; Geudtner, G.; et al. Molecular Simulations with in-deMon2k QM/MM, a Tutorial-Review. *Molecules* **2019**, *24* (9), 1653.

(20) Tzeliou, C. E.; Mermigki, M. A.; Tzeli, D. Review on the QM/MM Methodologies and Their Application to Metalloproteins. *Molecules* **2022**, *27* (9), 2660.

(21) Amin, M.; Mohamed, Z.; El-Sayed, M.; Samy, A.; Sultan, A.; Bassuoni, M.; Alkordi, M. H. Combined QM/MM and Monte Carlo study for redox leveling in Mn and Fe superoxide dismutase. *J. Biol. Inorg. Chem.* **2018**, *23* (2), 285−293.

(22) Torres, R. A.; Lovell, T.; Noodleman, L.; Case, D. A. Density functional and reduction potential calculations of Fe4S4 clusters. *J. Am. Chem. Soc.* **2003**, *125* (7), 1923−1936.

(23) Kapuscinska, K.; Dukala, Z.; Doha, M.; Ansari, E.; Wang, J.; Brudvig, G. W.; Brooks, B.; Amin, M. Bridging the Coordination Chemistry of Small Compounds and Metalloproteins Using Machine Learning. *J. Chem. Inf Model* **2024**, *64* (7), 2586−2593.

(24) Dauter, Z.; Wilson, K. S.; Sieker, L. C.; Moulis, J. M.; Meyer, J. Zinc- and iron-rubredoxins from Clostridium pasteurianum at atomic resolution: a high-precision model of a ZnS4 coordination unit in a protein. *Proc. Natl. Acad. Sci. U. S. A.* **1996**, *93* (17), 8836−8840.

(25) Bonisch, H.; Schmidt, C. L.; Schafer, G.; Ladenstein, R. The structure of the soluble domain of an archaeal Rieske iron-sulfur protein at 1.1 A resolution. *J. Mol. Biol.* **2002**, *319* (3), 791−805.

(26) Henninger, T.; Anemüller, S.; Fitz-Gibbon, S.; Miller, J. H.; Schäfer, G.; Schmidt, C. L. A Novel Rieske Iron-Sulfur Protein from the Hyperthermophilic Crenarchaeon Pyrobaculum aerophilum:

Sequencing of the Gene, Expression in E. coli and Characterization of the Protein. *Journal of Bioenergetics and Biomembranes* **1999**, *31* (2), 119−128.
(27) Hunsicker-Wang, L. M.; Heine, A.; Chen, Y.; Luna, E. P.; Todaro, T.; Zhang, Y. M.; Williams, P. A.; McRee, D. E.; Hirst, J.; Stout, C. D.; et al. High-resolution structure of the soluble, respiratory-type Rieske protein from Thermus thermophilus: analysis and comparison. *Biochemistry* **2003**, *42* (24), 7303−7317.
(28) Hunsicker-Wang, L. M.; Heine, A.; Chen, Y.; Luna, E. P.; Todaro, T.; Zhang, Y. M.; Williams, P. A.; McRee, D. E.; Hirst, J.; Stout, C. D.; et al. High-Resolution Structure of the Soluble, Respiratory-Type Rieske Protein from Thermus thermophilus: Analysis and Comparison. *Biochemistry* **2003**, *42* (24), 7303−7317.
(29) Morales, R.; Charon, M. H.; Hudry-Clergeon, G.; Petillot, Y.; Norager, S.; Medina, M.; Frey, M. Refined X-ray structures of the oxidized, at 1.3 A, and reduced, at 1.17 A, [2Fe-2S] ferredoxin from the cyanobacterium Anabaena PCC7119 show redox-linked conformational changes. *Biochemistry* **1999**, *38* (48), 15764−15773.
(30) Carrell, C. J.; Zhang, H.; Cramer, W. A.; Smith, J. L. Biological identity and diversity in photosynthesis and respiration: structure of the lumen-side domain of the chloroplast Rieske protein. *Structure* **1997**, *5* (12), 1613−1625.
(31) Carrell, C. J.; Zhang, H.; Cramer, W. A.; Smith, J. L. Biological identity and diversity in photosynthesis and respiration: structure of the lumen-side domain of the chloroplast Rieske protein. *Structure* **1997**, *5* (12), 1613−1625.
(32) Kolling, D. J.; Brunzelle, J. S.; Lhee, S.; Crofts, A. R.; Nair, S. K. Atomic resolution structures of rieske iron-sulfur protein: role of hydrogen bonds in tuning the redox potential of iron-sulfur clusters. *Structure* **2007**, *15* (1), 29−38.
(33) Correll, C. C.; Batie, C. J.; Ballou, D. P.; Ludwig, M. L. Phthalate dioxygenase reductase: a modular structure for electron transfer from pyridine nucleotides to [2Fe-2S]. *Science* **1992**, *258* (5088), 1604−1610.
(34) Baxter, E. L.; Zuris, J. A.; Wang, C.; Vo, P. L.; Axelrod, H. L.; Cohen, A. E.; Paddock, M. L.; Nechushtai, R.; Onuchic, J. N.; Jennings, P. A. Allosteric control in a metalloprotein dramatically alters function. *Proc. Natl. Acad. Sci. U. S. A.* **2013**, *110* (3), 948−953.
(35) Tamir, S.; Eisenberg-Domovich, Y.; Conlan, A. R.; Stofleth, J. T.; Lipper, C. H.; Paddock, M. L.; Mittler, R.; Jennings, P. A.; Livnah, O.; Nechushtai, R. A point mutation in the [2Fe-2S] cluster binding region of the NAF-1 protein (H114C) dramatically hinders the cluster donor properties. *Acta Crystallogr., Sect. D: Biol. Crystallogr.* **2014**, *70* (Pt6), 1572−1578.
(36) Kishimoto, H.; Azai, C.; Yamamoto, T.; Mutoh, R.; Nakaniwa, T.; Tanaka, H.; Miyanoiri, Y.; Kurisu, G.; Oh-Oka, H. Soluble domains of cytochrome c-556 and Rieske iron-sulfur protein from Chlorobaculum tepidum: Crystal structures and interaction analysis. *Curr. Res. Struct Biol.* **2023**, *5*, No. 100101.
(37) Kissinger, C. R.; Sieker, L. C.; Adman, E. T.; Jensen, L. H. Refined crystal structure of ferredoxin II from Desulfovibrio gigas at 1.7 A. *J. Mol. Biol.* **1991**, *219* (4), 693−715.
(38) Stout, C. D. Crystal structures of oxidized and reduced Azotobacter vinelandii ferredoxin at pH 8 and 6. *J. Biol. Chem.* **1993**, *268* (34), 25920−25927.
(39) Parisini, E.; Capozzi, F.; Lubini, P.; Lamzin, V.; Luchinat, C.; Sheldrick, G. M. Ab initio solution and refinement of two high-potential iron protein structures at atomic resolution. *Acta Crystallogr., Sect. D: Biol. Crystallogr.* **1999**, *55* (Pt 11), 1773−1784.
(40) Sery, A.; Housset, D.; Serre, L.; Bonicel, J.; Hatchikian, C.; Frey, M.; Roth, M. Crystal structure of the ferredoxin I from Desulfovibrio africanus at 2.3 A resolution. *Biochemistry* **1994**, *33* (51), 15408−15417.
(41) Strop, P.; Takahara, P. M.; Chiu, H.; Angove, H. C.; Burgess, B. K.; Rees, D. C. Crystal structure of the all-ferrous [4Fe-4S]0 form of the nitrogenase iron protein from Azotobacter vinelandii. *Biochemistry* **2001**, *40* (3), 651−656.
(42) Tan, M. L.; Perrin, B. S., Jr.; Niu, S.; Huang, Q.; Ichiye, T. Protein dynamics and the all-ferrous [Fe4 S4] cluster in the nitrogenase iron protein. *Protein Sci.* **2016**, *25* (1), 12−18.
(43) Fukuyama, K.; Okada, T.; Kakuta, Y.; Takahashi, Y. Atomic resolution structures of oxidized [4Fe-4S] ferredoxin from Bacillus thermoproteolyticus in two crystal forms: systematic distortion of [4Fe-4S] cluster in the protein. *J. Mol. Biol.* **2002**, *315* (5), 1155−1166.
(44) Jordan, P.; Fromme, P.; Witt, H. T.; Klukas, O.; Saenger, W.; Krauss, N. Three-dimensional structure of cyanobacterial photosystem I at 2.5 A resolution. *Nature* **2001**, *411* (6840), 909−917.
(45) Macedo-Ribeiro, S.; Darimont, B.; Sterner, R.; Huber, R. Small structural changes account for the high thermostability of 1[4Fe-4S] ferredoxin from the hyperthermophilic bacterium Thermotoga maritima. *Structure* **1996**, *4* (11), 1291−1301.
(46) Li, B.; Steindel, P.; Haddad, N.; Elliott, S. J. Maximizing (Electro)catalytic CO2 Reduction with a Ferredoxin-Based Reduction Potential Gradient. *ACS Catal.* **2021**, *11* (7), 4009−4023.
(47) Breiter, D. R.; Meyer, T. E.; Rayment, I.; Holden, H. M. The molecular structure of the high potential iron-sulfur protein isolated from Ectothiorhodospira halophila determined at 2.5-A resolution. *J. Biol. Chem.* **1991**, *266* (28), 18660−18667.
(48) Takeda, K.; Kusumoto, K.; Hirano, Y.; Miki, K. Detailed assessment of X-ray induced structural perturbation in a crystalline state protein. *J. Struct Biol.* **2010**, *169* (2), 135−144.
(49) Baranovskiy, A. G.; Zhang, Y.; Suwa, Y.; Babayeva, N. D.; Gu, J.; Pavlov, Y. I.; Tahirov, T. H. Crystal structure of the human primase. *J. Biol. Chem.* **2015**, *290* (9), 5635−5646.
(50) O'Brien, E.; Holt, M. E.; Salay, L. E.; Chazin, W. J.; Barton, J. K. Substrate Binding Regulates Redox Signaling in Human DNA Primase. *J. Am. Chem. Soc.* **2018**, *140* (49), 17153−17162.
(51) Hanazono, Y.; Hirano, Y.; Takeda, K.; Kusaka, K.; Tamada, T.; Miki, K. Revisiting the concept of peptide bond planarity in an iron-sulfur protein by neutron structure analysis. *Sci. Adv.* **2022**, *8* (20), No. eabn2276.
(52) Brown, I. D. Recent developments in the methods and applications of the bond valence model. *Chem. Rev.* **2009**, *109* (12), 6858−6919.
(53) Brown, I. D. What is the best way to determine bond-valence parameters? *IUCrJ.* **2017**, *4* (Pt5), 514−515.
(54) Liu, J.; Chakraborty, S.; Hosseinzadeh, P.; Yu, Y.; Tian, S.; Petrik, I.; Bhagi, A.; Lu, Y. Metalloproteins containing cytochrome, iron-sulfur, or copper redox centers. *Chem. Rev.* **2014**, *114* (8), 4366−4469.
(55) Schroder, G. F.; Levitt, M.; Brunger, A. T. Super-resolution biomolecular crystallography with low-resolution data. *Nature* **2010**, *464* (7292), 1218−1222.
(56) Shapovalov, M. V.; Dunbrack, R. L., Jr. Statistical and conformational analysis of the electron density of protein side chains. *Proteins* **2007**, *66* (2), 279−303.
(57) Atkinson, J. T.; Campbell, I.; Bennett, G. N.; Silberg, J. J. Cellular Assays for Ferredoxins: A Strategy for Understanding Electron Flow through Protein Carriers That Link Metabolic Pathways. *Biochemistry* **2016**, *55* (51), 7047−7064.
(58) Sticht, H.; Rosch, P. The structure of iron-sulfur proteins. *Prog. Biophys. Mol. Biol.* **1998**, *70* (2), 95−136.
(59) Campbell, I. J.; Kahanda, D.; Atkinson, J. T.; Sparks, O. N.; Kim, J.; Tseng, C. P.; Verduzco, R.; Bennett, G. N.; Silberg, J. J. Recombination of 2Fe-2S Ferredoxins Reveals Differences in the Inheritance of Thermostability and Midpoint Potential. *ACS Synth. Biol.* **2020**, *9* (12), 3245−3253.
(60) Vallieres, C.; Benoit, O.; Guittet, O.; Huang, M. E.; Lepoivre, M.; Golinelli-Cohen, M. P.; Vernis, L. Iron-sulfur protein odyssey: exploring their cluster functional versatility and challenging identification. *Metallomics* **2024**, *16* (5), No. mfae025.

https://doi.org/10.1021/acsomega.5c01976
ACS Omega 2025, 10, 15790−15798